Observation of high-pressure polymorphs in bulk silicon formed at relativistic laser intensities

Ludovic Rapp [1,*,†] Takeshi Matsuoka,[2,*] Konstantin L. Firestein [3] Daisuke Sagae,[4] Hideaki Habara [4] Keiichiro Mukai,[4] Kazuo A. Tanaka,[4] Eugene G. Gamaly [1] Ryosuke Kodama,[4,5] Yusuke Seto,[6] Takahisa Shobu,[7] Aki Tominaga [8] Lachlan Smillie,[1,‡] Tatiana Pikuz,[2] Bianca Haberl,[9] Toshinori Yabuuchi,[10,11] Tadashi Togashi [10,11] Yuichi Inubushi,[10,11] Makina Yabashi,[10,11] Saulius Juodkazis [12,13] Dmitri V. Golberg,[3] Andrei V. Rode [1] and Norimasa Ozaki[4,5,§]

[1]*Laser Physics Centre, Department of Quantum Science and Technology, Research School of Physics, The Australian National University, Canberra, Australian Capital Territory 2601, Australia*
[2]*Institute for Open and Transdisciplinary Research Initiatives, Osaka University, Suita, Osaka 565-0871, Japan*
[3]*Centre for Materials Science and School of Chemistry and Physics, Queensland University of Technology, Brisbane, Queensland 4000, Australia*
[4]*Graduate School of Engineering, Osaka University, Suita, Osaka 565-0871, Japan*
[5]*Institute of Laser Engineering, Osaka University, Suita, Osaka 565-0871, Japan*
[6]*Graduate School of Science, Kobe University, Kobe, Hyogo 657-8501, Japan*
[7]*Japan Atomic Energy Agency, Chiyoda-ku, Tokyo 100-8577, Japan*
[8]*Materials Science Research Center, Japan Atomic Energy Agency, Kouto, Hyogo 679-5148, Japan*
[9]*Neutron Scattering Division, Neutron Sciences Directorate, Oak Ridge National Laboratory, Oak Ridge 37831, USA*
[10]*Japan Synchrotron Radiation Research Institute, Sayo, Hyogo 679-5198, Japan*
[11]*RIKEN SPring-8 Center, Sayo, Hyogo 679-5148, Japan*
[12]*Optical Sciences Centre and ARC Training Centre in Surface Engineering for Advanced Materials (SEAM), School of Science, Swinburne University of Technology, Hawthorn, Victoria 3122, Australia*
[13]*Tokyo Tech World Research Hub Initiative (WRHI), School of Materials and Chemical Technology, Tokyo Institute of Technology, Tokyo 152-8550, Japan*

Silicon polymorphs with exotic electronic and optical properties have recently attracted significant attention due to their wide range of useful band gap characteristics. They are typically formed by static high-pressure techniques, which limits the crystal structures that can be made. This constitutes a major obstacle to study these polymorphs and their incorporation into existing technology. Approaches have attempted to address this shortcoming through using dynamic conditions and chemical precursor materials. Here, we report on an approach to create unusual crystal structures deep in the bulk of a silicon crystal by irradiating it with a laser pulse at ultrarelativistic intensity of up to 7.5×10^{19} W/cm^2. Laser-generated electrons with MeV energy swiftly penetrate the target with speed close to the speed of light and deposit their energy into a large volume across the whole thickness of the sample. The relativistic electron current creates, via branching propagation and ionization, high-energy-density conditions for thermodynamically nonequilibrium phase transformation paths into new crystal polymorphs. X-ray microdiffraction and synchrotron x-ray diffraction analyses indicate, along with conventional dc-Si, the presence of exotic silicon structures in the bulk of the laser intact target volume. These structures are identified as body-centered bc8-Si, rhombohedral r8-Si, hexagonal-diamond hd-Si, and the tetragonal Si-VIII, all phases of Si that have previously been made through static techniques. Additionally, simple-tetragonal st12-Si and body-centered tetragonal bt8-Si were observed along with signatures of not yet identified diffraction spots. Both st12-Si and bt8-Si have only been observed in ultrafast laser microexplosion conditions at much lower laser intensity $\sim 10^{14}$ W/cm^2 and within a micron-thin surface layer. The findings here are supported by direct observation of nanoparticles with high-resolution transmission electron microscopy and corresponding fast Fourier transform analysis of their interatomic distances. The presented analyses of absorbed laser energy, generation of the MeV electron current, and deposition of energy across the whole target thickness provide a solid basis for drawing the conclusion that the observed silicon polymorphs were produced because of

*These authors contributed equally to this work.

†ludovic.rapp@anu.edu.au

‡Currently at the University of Wollongong, Wollongong, New South Wales 2522, Australia.

§norimasa.ozaki@eie.eng.osaka-u.ac.jp

laser-generated high-energy electrons fast-penetrating deeply into the bulk of silicon. In contrast to solid-solid transformations, the plasma-solid transitions offer a paradigm for the creation of exotic, high-energy density materials inside the bulk of the sample by using laser pulses at relativistic intensities.

I. INTRODUCTION

Silicon (Si) is the second, after oxygen, most abundant element on our planet and is of utmost technological importance as the foundation stone in the semiconductor industry. While widely adopted for many electronic and optical purposes, there exist many widespread applications where silicon is not applicable due to limits imposed by its normal diamond-cubic (dc) phase band structure. When exposed to extreme conditions silicon atoms can rearrange into new crystal structures. Initial compression to ∼11 GPa yields a metallic polymorph with so-called β-Sn structure [1,2], with a series of further metallic high-pressure polymorphs forming upon continued pressurization [1]. Interestingly, the energy landscape of Si at extreme pressure and temperature is rich with local minima, and upon decompression, phase transitions are not necessarily reversible. Instead, full pressure release can yield polymorphs exhibiting unusual optical and electronic properties [1–4], whereby the new phases can be recovered metastably to ambient conditions [4–17]. These metastable, exotic Si phases have a wide range of electronic properties, which are determined by the diversity of their atomic structures [7–9,18–20]. In the search for such structures, metastable and recoverable to ambient conditions, many highly useful allotropes of Si were predicted, especially allotropes for photovoltaic applications [7,18–21] due to their absorption in the infrared spectral range. This suggests that more may also be kinetically stable at ambient conditions.

The transformation of Si under megabar pressures (and in some cases additional high temperature) was studied in static conditions, in a diamond anvil cell (DAC) [3], and in dynamic conditions, using strong shock waves generated by explosives and megajoule-class nanosecond pulse lasers [22]. Interestingly, the synthesis of the exotic, metastable phases recoverable to ambient conditions does not require megabar pressures but often only somewhat >10 GPa. This has opened the door to large-volume synthesis. For example, pressure release from the metallic β-Sn structure yields r8-Si [14], followed by the so-called bc8 phase, a metastable phase of Si [1,4]. This bc8-Si has been produced in large volumes via solid-solid transformation using the multianvil press method which allowed reliable measurements of their optical and band gap properties [21]. Another silicon allotrope Si_{24} with a quasidirect band gap was synthesized through a high-pressure precursor process in a multianvil press [9,23]. Further solid-solid transition into hexagonal $4H$-Si has been demonstrated by annealing large volumes of Si_{24} and bc8-Si [24,25].

In addition to large-volume synthesis, relatively moderate pressures have also enabled investigation of kinetic effects due to varying decompression rates. For example, an early study identified two metastable phases, Si-VIII and Si-XIX, following rapid decompression from metallic Si using a DAC specifically set up with a Belleville spring and screw [6]. More recently, a double-membrane setup for a conventional

DAC showed that rapid decompression can avoid the r8/bc8 pathway. Instead, an amorphous structure with a residual of β-Sn was found upon full decompression to ambient [26].

However, the synthesis of metastable phases by standard DACs is naturally limited by the strength of the diamond and the rate at which pressure can be applied and released. In direct laser-driven shock-wave compression, the flexibility of adjusting laser pulse energy, duration, and the ability to control temporal and spatial intensity distribution allow for precisely controlling the shock-wave loading to probe different thermodynamic states. These studies have uncovered the high-pressure equation of state and isentropic sound speed up to 2.1 TPa [22]. The phase transitions into high-pressure polymorphs are evident from the velocity interferometry and from time-resolved x-ray diffraction (XRD) patterns obtained with the x-ray free electron laser probe. Very recent nanosecond laser-driven shock-wave compression- and decompression-generated ultrahigh strain rates at 10^{12} W/cm² laser intensity combined with time-resolved XRD patterns using an ultrafast x-ray probe demonstrate *in situ* the dynamics of phase transitions with nanosecond time resolution, resolving the longstanding controversy on silicon deformation. These provide direct proof of strain-rate–dependent deformation mechanisms in the silicon structure, reveal insight into the relationship between dc-Si and metallic phases, and show that metallic β-Sn can be maintained down to ambient pressure [27]. However, the few-nanosecond lifetime of the so-created high-pressure polymorphs is too short for practical utilization. While DAC and shock-wave compression studies yield unparalleled insight into transition behaviors and phase diagrams, they do not yield materials in a geometry that is readily incorporated into the semiconductor wafer-based technology.

Recently, a powerful method to form extreme conditions was developed and combined the best of both worlds, namely, the ultrashort pulse laser-induced microexplosion and confined geometry [28–31]. Just 1 µJ of energy delivered from an ultrashort laser pulse focused into a submicron volume (focal volume of <1 µm³) within a time <1 ps (1 ps = 10^{-12} s) immediately leads to an energy density >1 MJ/cm³ [28,29], resulting in a maximum pressure at the shock-wave front of 1 TPa, higher than the strength of any material, and temperatures > 10^5 K. The essential detail here is that the energy of the electromagnetic field of laser radiation is deposited into the electron subsystem faster than it can be transferred to the lattice through the electron-ion collisions and electronic heat conduction [22–30,32], which is typically in the time scale of a few picoseconds. The plasma-solid transformation from the thermodynamically nonequilibrium high-entropy state of warm dense matter [33] is favorable for the formation on metastable phases during fast cooling from such a hot, extremely dense plasma, which helps to overcome kinetic barriers to the formation of specific metastable phases and thus cannot be formed in solid-solid transformation and in shock compression with MJ nanosecond laser transfor-

mation methods. By focusing ultrashort laser pulses on a Si surface buried under a 10-μm-thick oxidized layer for creating confined geometry conditions [10,11], two energetically competitive tetragonal structures were identified in the laser-modified volume by electron diffraction and complementary *ab initio* random structure searches [10,34]. These were the so-called st12-Si, an analogous structure to the well-known st12 phase of germanium, and the bt8-Si structure. While bt8-Si is predicted to be a narrow-band-gap semiconductor [10], st12-Si was calculated to have an indirect band gap of 1.1 eV within density functional theory (DFT, which could imply the typical underestimation of the gap) with potentially interesting properties for exploring Si-based superconductivity [35]. In addition, electron diffraction revealed the presence of other yet unidentified Si phases. None of these phases have yet been synthesized by static techniques, although particularly st12-Si could exhibit critical technological advantages due to its band gap characteristics and expected thermal stability. Furthermore, all these transformations occurred in nanovolumes contained within a thin surface layer, up to 1 μm deep in the bulk only. Estimates from transmission electron microscopy (TEM) images [10] suggest that the amount of new phase produced in a single laser shot with <1 μJ energy at $\sim 10^{14}$ W/cm^2 is of the order of $\sim 10^{-15}$ to 10^{-14} g, which makes it extremely difficult to further characterize its electronic properties or assess its thermal stability. This bottleneck has indeed been a major inhibitor toward the practical use of these intriguing Si polymorphs. Thus, to increase the number of atoms converted into these unconventionally structured crystal lattices, the development of a method altering a much larger volume of Si structure is required, specifically a method that deposits energy into the electrons faster than it can be transferred to the ions.

In this paper, we report on a way to create unusual crystal structures in much larger volumes, perhaps up to $\sim 7 \times 10^{-6}$ g in mass, deep in the bulk of a silicon wafer via the distribution of absorbed laser energy by MeV electrons generated at ultrarelativistic intensities [36–39] up to 7.5×10^{19} W/cm^2. Electrons with MeV kinetic energy and relativistic velocities close to the speed of light, which results in an increase of the electron mass [33,39], penetrate deep into the bulk and counterintuitively divide, due to interelectronic repulsion and its self-induced magnetic field, to produce a branched flow across the silicon bulk [40–42]. The MeV electrons loose off their energy via collisions and ionization of atoms [43–45], which then allow the atoms to move from their equilibrium positions and restructure into new metastable crystal arrangements. The branched propagation, in addition to the recoil pressure, allows the formation of the observed high-pressure Si phases deep in the large volume of the target bulk.

To assess repeatability and consistency of this approach, we exposed seven Si targets in total, whereby three samples were exposed below and four samples above the relativistic intensity threshold of 2.15×10^{18} W/cm^2. For each sample, pulse duration and focal spot size were set the same, and the laser intensity was changed by varying the pulse energy. Reproducibility was evaluated through subjecting all seven samples to the same detailed analysis, and all of those above the threshold demonstrate a similar presence of high-pressure phases.

As a result, we demonstrate the conversion of the silicon target into new silicon polymorphs. This synthesis includes the formation of st12-Si and bt8-Si, the intriguing phases that were previously only made by confined microexplosions and that have not been made by static techniques. Here, we find considerably greater quantities of these two intriguing phases than previously achieved by laser-processing in confined [10,11] geometry and all preserved in the crystal matrix. This is an important advance for exotic Si materials from the previous synthesis method, which may open a route to the fabrication and investigation of other high-pressure materials and a potential roadmap toward tailored band-gap engineering.

II. EXPERIMENTAL OBSERVATIONS

A. Irradiation of silicon sample at relativistic intensity

Powerful 25 fs laser single pulses with a wavelength $\lambda = 800$ nm and energy up to ~ 1 J were tightly focused on the surface of Si crystals at $53.4°$ to the normal of the target surface to form a focal spot of 3×14 μm full width at half maximum (FWHM) to achieve the laser irradiation intensity up to 7.5×10^{19} W/cm^2 at maximum pulse energy of 0.62 J. The highest intensity in the experiments was well above the relativistic intensity threshold of 2.15×10^{18} W/cm^2 for 800 nm laser wavelength, see Sec. S-I in Supplemental Material [46] for details. Visual inspection of samples after the experiment showed that a rather large amount of material had been ablated from the front surface (Fig. 1). Those irradiated by pulse intensity 7.5×10^{19} W/cm^2 demonstrated spallation at the rear surface, while none was observed at lower intensities. This is an indication that a significant amount of energy was delivered to the rear surface of the 525-μm-thick silicon crystal.

The effect of spallation is illustrated in Fig. 1, where optical images of the front and rear surfaces of the sample irradiated with 0.62 J pulse are shown. The maximum depth of the ablated crater reached 175 μm for a volume measured at 8.72 $\times 10^7$ μm^3, and the spalled crater is up to ~ 106 μm deep with a volume of 1.89×10^7 μm^3. In this sample, there are clearly visible cracks in the crystal spreading away from the craters. That gave us an opportunity to analyze and characterize the material not only on the crater and spallation floors but also within the volume between the ablated and spalled craters.

A significant, about two orders of magnitude, increase in the ablated crater volume is clearly seen in Fig. 1(h) as soon as the laser intensity passes the relativistic intensity threshold at 2×10^{18} W/cm^2, see also Fig. S-02 and Table S-01 in Supplemental Material [46]. We attribute this increase to the generation of relativistic electrons swiftly penetrating and depositing their energy through the whole thickness of silicon sample, see Discussion below.

B. Localization of Si phases by Raman microspectroscopy

The floor surfaces of the ablated and spalled craters were examined by confocal Raman spectroscopy. We note here that the new Si allotropes may only be visible when and only if they are present in a sufficiently large, >100 nm, fraction of the sampled material [11,47]. Further, only Si allotropes with a band gap can readily be detected with Raman spectroscopy in such small samples. If structures are present under high
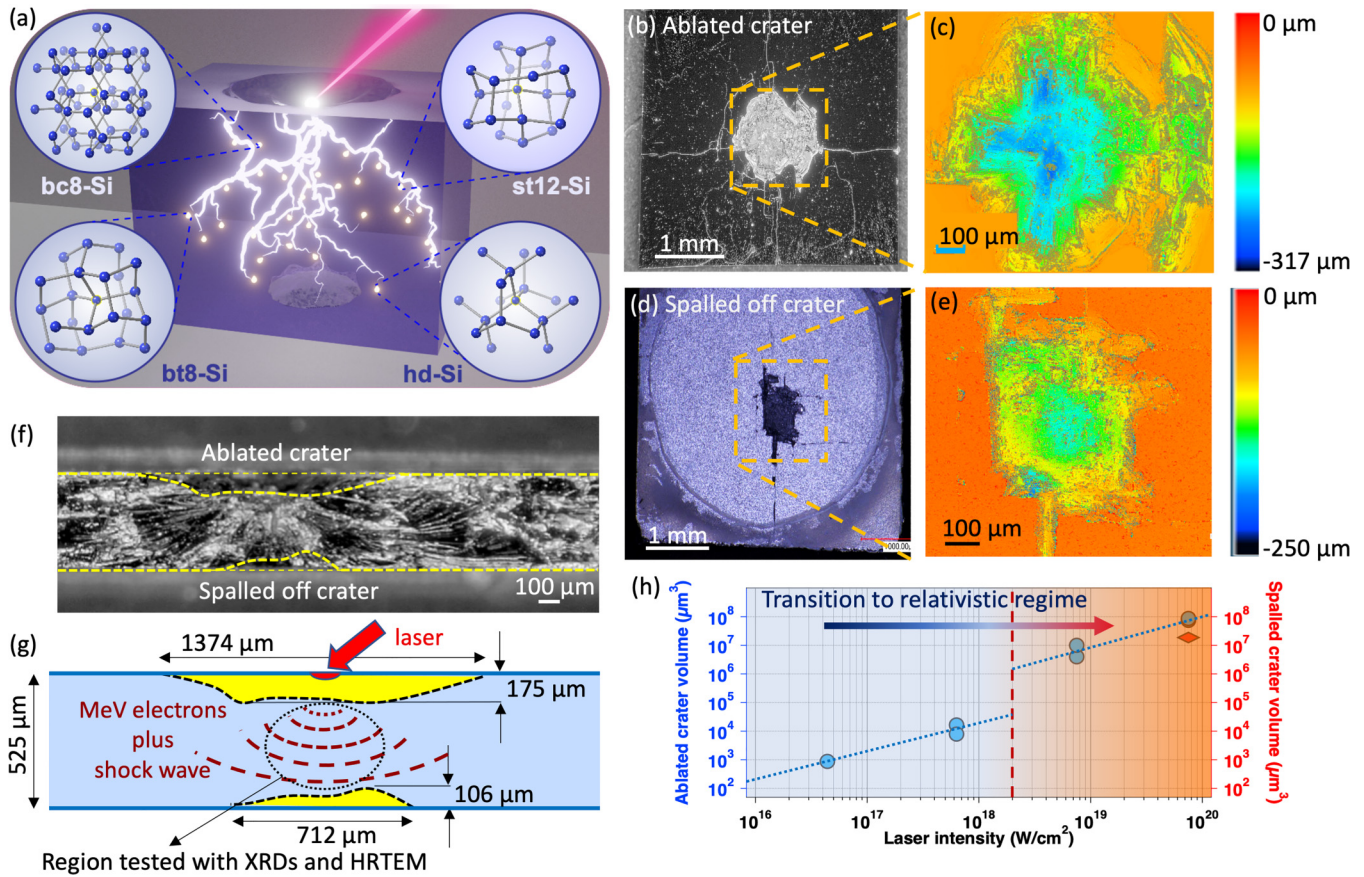
FIG. 1. Ablation and spallation craters in Si sample. (a) Schematic representation of irradiation of a target by a laser pulse, generation of relativistic electrons, their branching in Si bulk, and resulting formation of high-pressure Si-polymorphs. Optical microscopy images of the (b) ablated and (d) spalled craters and their spatial profilometer mappings formed at the (c) front and (e) rear surfaces of a 525-μm-thick Si sample exposed to a 25-fs-ultrashort laser pulse at the intensity of 7.5×10^{19} W/cm^2. (f) Side view of the sample cracked through the middle of the craters and (g) schematic representation of the ablated and spalled craters indicating the removed volume in yellow. The circle indicates the region tested with micro-x-ray diffraction (XRD), synchrotron XRD, and high-resolution transmission electron microscopy (HRTEM). (h) The dependency of the ablated (blue circles) and spalled (red diamond) volumes on laser pulse intensity. The relativistic intensity threshold at 2.15×10^{18} W/cm^2 is indicated by a red vertical dash line. The blue dotted lines are guides to the eye indicating the ablated volume trends below and above the relativistic threshold. Note the distinctive jump in ablated volume in (h) at the intensity levels above the relativistic threshold.

stress so that band gaps are reduced to naught, they may thus not be detected.

Two types of modification were observed in the Raman spectra (see Appendix 3 for details), namely, the shift of Raman peaks from their known unstrained positions and the presence of peaks attributed to exotic Si phases. These notable changes are observed on the ablated crater floor in a sample irradiated at 7.5×10^{18} W/cm^2; comparable results are found in the samples irradiated at 7.5×10^{19} W/cm^2 and on the surface of the crack in between the ablated and spalled craters [Fig. 1(f)]. However, Raman spectra taken from the spalled crater surface [Figs. 1(d) and 1(e)] indicated only the presence of the original unstressed dc-Si structure.

The spectrum in Fig. 2 contains both disordered Si, indicated by amorphouslike transverse acoustic (TA, a-Si) bands, the typical transverse optic (TO) band of dc-Si and the 2TA band of dc-Si. The dc-Si TO peak is also observed to be shifted from its unstrained dc-Si position at 520.5 cm^{-1}, depending on the local test position. The shift up to 522.7 cm^{-1}

can be explained by a compressive stress, which causes the TO band of dc-Si to shift to higher wave numbers. It is indicative of a local residual compressive strain equivalent to a pressure range from 0.7 to 1.0 GPa [49,50]. Shifts from 520.5 cm^{-1} to lower wave numbers, down to 507.1 cm^{-1}, were also observed. These could be attributed to tensile stress and/or nanocrystallinity [50,51].

Two additional peaks at ∼353 and 438 cm^{-1} are commonly associated with Si phases recovered from high pressure, most typically with the cubic bc8-Si and the rhombohedral r8-Si structures [8,11,18], but also with bt8-Si [10]. Note that the bc8-Si structure typically transforms from r8-Si as Si fully decompresses from high pressure [7,14], but both together have been readily observed under phase transitions induced through indentation methods [8].

Raman spectra collected from the surface of cracks between the ablated and spalled craters shown in Fig. 1(f) served as an indication of the presence of unusual silicon polymorphs across the thickness of the whole sample. With only two
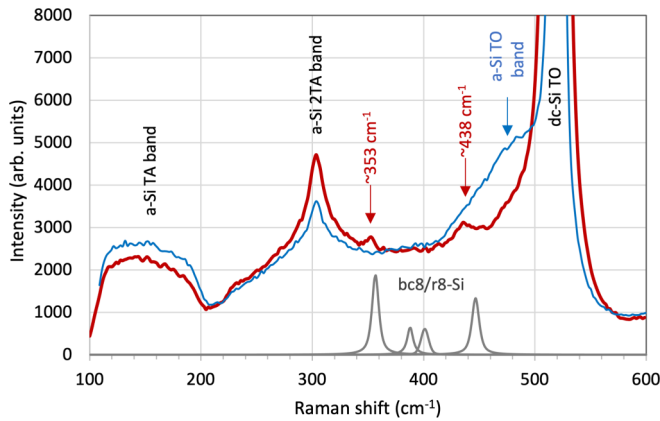
FIG. 2. Raman spectra. The confocal microscope Raman scattering collected from local points on the surface of the cracks of laser-irradiated Si sample at 7.5×10^{19} W/cm^2, showing broad bands related to transverse acoustic (a-Si TA, a-Si 2TA) and optical phonons from amorphous Si and diamond-cubic Si (a-Si TO, dc-Si TO). The red line spectrum indicates the presence of additional peaks at $\sim$353 and $\sim$438 cm^{-1} from crystalline metastable phases bc8/r8-Si on top of amorphous (a-Si) bands. The blue line spectrum is from a different local test on the same surface without these peaks but with increased intensity from amorphous Si spectra (a-Si TO band). The gray peaks are simulated bc8/r8-Si Raman spectra in 300–500 cm^{-1} [11,48].

relatively weak intensity peaks on top of conventional Raman spectra from disordered and crystalline Si, it is not possible to confidently associate these peaks specifically to the bc8-Si, bt8-Si, or r8-Si phase.

C. X-ray microdiffraction

The two-dimensional (2D) patterns from x-ray microdiffraction of the sample area of interest and one-dimensional (1D) pattern integrated from 2D are shown in Fig. 3. XRD analysis of the sample irradiated by 0.62 J laser pulse (intensity 7.5×10^{19} W/cm^2 or $\sim$35 times above the relativistic threshold) reveals that, apart from the peaks originated from conventional dc-Si, additional XRD peaks are seen at 2θ of 32.27°, 33.51°, and 35.35° (interplanar distances $d =$ 2.77, 2.67, and 2.54 Å, respectively). Such angles correspond reasonably well to the d spacings in several metastable phases, for instance, of the bc8 phase (space group $Ia3$, $a =$ 6.636 Å) $d_{[211]} = 2.71$ Å as well as the bt8 phase (space group $I4_1/a$, $a = 6.676$ Å, $c = 6.522$ Å) $d_{[112]} = 2.68$ Å, for the st12 phase (space group $P4_3 2_1 2$, $a = 5.678$ Å, $c = 6.825$ Å) $d_{[201]} = 2.62$ Å and $d_{[210]} = 2.54$ Å [4,9,10].

The results of the microdiffraction tests serve as an independent indication of the presence of pressure-induced polymorphs in the bulk of Si. We performed further XRD analysis of the laser-irradiated samples with synchrotron radiation and with high-resolution TEM (HRTEM) imaging, which we present in the following sections.

D. Evidence of high-pressure phases from synchrotron XRD

Synchrotron XRD characterization with a beam energy of 30.047 ± 0.048 keV of samples irradiated by a laser pulse
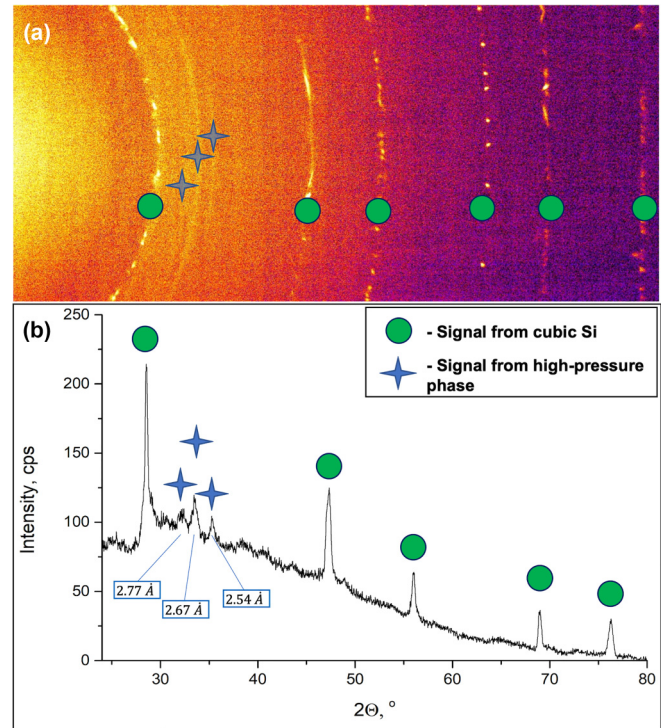

FIG. 3. X-ray microdiffraction analysis with Cu-$K\alpha$ radiation. (a) Two-dimensional (2D) patterns of x-ray diffraction of the area of Si sample between the ablated and spalled craters. (b) One-dimensional (1D) spectral pattern integrated from the 2D data shown in (a). Adapted from Ref. [50] with permission.

was performed in the end station of the BL22XU beamline in SPring8 synchrotron. A total of 516 XRD images have been analyzed, wherein 402 diffraction patterns showed from 2 up to 8 diffraction spots different from those from the original dc-Si structure.

The XRD data indicate the presence of unusual Si structures within the large Si sample volume probed here. Figure 4 presents the results with the sample irradiated at 7.5×10^{18} W/cm^2, 10 times lower than the maximum intensity available in the experiments. The multitude of different reflections detected across the entire set of XRD data do not just correspond to one known Si phase but most likely several. These structures are potentially the tetragonal bt8-Si ($I4_1/a$ space group) or the body-centered cubic bc8-Si (Ia-3 space group). Further, the presence of rhombohedral r8-Si (R-3 space group), simple-tetragonal st12-Si ($P4_3 2_1 2$ space group), hexagonal diamond/lonsdaleite hd-Si ($P63/mmm$ space group), and the tetragonal Si-VIII cannot be excluded, see Table I. Each of the structures has uniquely identified reflections, which cannot be attributed to any other structure. In addition, several reflections with question marks in Table I indicate those measured d spacings that cannot be attributed to any known phase of silicon polymorphs.

There is a notable number of observed reflections that cannot be reliably assigned to the interatomic spacings of the known polymorph structures at ambient pressure. One of the possible reasons is the presence of considerable residual stress within this bulk sample. To identify the observed crystal spots,

TABLE I. XRD results. Experimental interatomic distances d in Å and the related identified Si polymorphs from the detected synchrotron XRD reflection (see Appendix 5 for the accuracy of measurements). The reflections shown in Fig. 4 are marked in the d-spacing column in bold. Question marks indicate the measured d spacings of yet unidentified structures. The last column indicates the number of times the reflection was detected in all XRD patterns for each of the interatomic distances. All crystal lattice parameters are given for unit cells at 0 GPa pressure.

Identified Si crystal structures with space groups $d \pm \Delta d$, (Å)	dc-Si $Fd-3m$ [52]	bc8-Si Ia-3 [4]	r8-Si R-3 [18]	st12-Si $P4_32_12$ [10]	bt8-Si $I4_1/a$ [10]	hd-Si $P6_3/mmc$ [15]	Si-VIII $P4_12_12$ [6]	No. reflection spots
Lattice parameters	$a = 5.4307$ Å	$a = 6.636$ Å	$a = 5.766$ Å $\gamma = 109.47°$	$a = 5.678$ Å $c = 6.825$ Å	$a = 6.676$ Å $c = 6.522$ Å	$a = 3.80$ Å $c = 6.28$ Å	$a = 8.627$ Å $c = 7.500$ Å	
3.277 ± 0.011						[100] 3.29 Å[a]		3
3.149 ± 0.010[b]		[111] 3.135 Å[b]				[002] 3.14 Å[b]		90[b]
2.774 ± 0.009	?[c]							78
2.765 ± 0.008	?[c]							69
2.733 ± 0.008							[310] 2.728 Å[a]	139
2.724 ± 0.008							[310] 2.728 Å[a]	94
2.715 ± 0.008 (**B, C, D**)			[110], [20−1] 2.718 Å[a]					100
2.707 ± 0.008 (**A**)		[211] 2.709 Å[a]						73
2.689 ± 0.008					[112] 2.683 Å		[301] 2.685 Å	41
2.664 ± 0.007	?[d]							10
2.646 ± 0.007	??							23
2.616 ± 0.007				[201] 2.621 Å[a]				144
2.552 ± 0.007	?[e]							23
2.226 ± 0.005	??							84
2.208 ± 0.005	??							70
2.185 ± 0.005 (**G**)				[022] 2.183 Å[a]				60
1.920 ± 0.005[b]		[220] 1.920 Å[b]		[221] 1.920 Å[b]				79[b]
1.906 ± 0.005						[110] 1.90 Å[a]		142
1.679 ± 0.004	?[f]							8
1.639 ± 0.003[b]		[311] 1.637 Å[b]						24[b]
1.400 ± 0.003 (**F**)				[133] 1.403 Å[a]				81
1.348 ± 0.003	??[g]							76
1.242 ± 0.002[b]		[331] 1.246 Å[b]				[210] 1.244 Å[b]		132[b]
1.213 ± 0.002 (**E, H**)[h]			[512] 1.212 Å[h]			[114] 1.210 Å[h]		14[h]
1.206 ± 0.002	??							48
1.200 ± 0.002	??							24
1.106 ± 0.002[b]		[422] 1.1085 Å[b]	[600] 1.106 Å[b]					118[b]
1.047 ± 0.002						[006] 1.047 Å[a]		48
0.959 ± 0.002						[901] 0.95 Å[a]		67

[a]Uniquely identified reflections at ambient pressure.

[b]Those reflections from dc-Si and possibly from other interatomic distances overlapping with dc-Si.

[c]Possible st12 [200] 2.839 Å at 0 GPa shrinks to 2.770 Å at 8 GPa [10].

[d]Possible bt8 [112] 2.683 Å at 0 GPa shrinks to 2.657 Å at 2 GPa [10].

[e]Possible st12 [112] 2.600 Å at 0 GPa shrinks to 2.547 Å at 4 GPa [10].

[f]Possible st12 [222] at 1.730 Å at 0 GPa shrinks to 1.678 Å at 8 GPa [10].

[g]Possible bt8 [422] 1.357 Å at 0 GPa shrinks to 1.347 Å at 2 GPa [10].

[h]Those reflections that could be assigned to two different crystal structures.

we used the previously obtained results [10] of an *ab initio* random structure searching computational search [34] with the CASTEP code [53]. Comparison of these previous searches with our current results shows that there are several, but not all, reflections that could be identified assuming that the bt8 and st12 polymorphs are at residual stresses of 2–8 GPa. There are still a few unidentified reflections indicated in Table I with question marks, which could result from not yet uncovered silicon structures. Indeed, beyond the more typical bc8-Si, r8-Si,

and hd-Si, several further pressure-induced polymorphs exist. These include bt8-Si, which we have previously demonstrated experimentally in laser-induced confined microexplosion conditions [10], the Si-VIII structure [6,17], and a range of other tetrahedral structures that might possibly form [10,18]. A very large number of other possible metastable Si phases have indeed been predicted. For example, simple consideration of the bc8-like family (which includes the known bc8, bt8, and r8) yields a further 128 tetrahedral structures with 16 (6 phases),
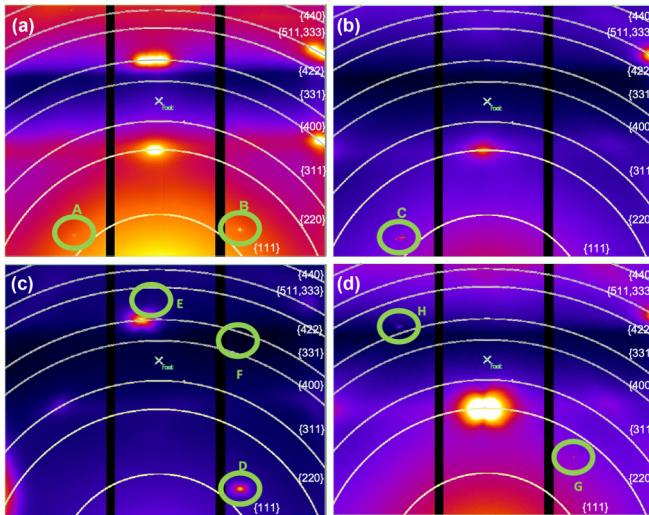
FIG. 4. Four representative x-ray diffraction (XRD) images of Si sample irradiated at a laser intensity of 7.5×10^{18} W/cm^2. The images are overlaid with arcs which show dc-Si interatomic distances indicated by [hkl] indices; the 2θ direction is radially outward. In each diffraction pattern, additional reflections are identified that correspond to exotic phases of Si, as indicated by a d spacing that is not dc-Si. (a) Spot A corresponding to 2.707 Å and spot B corresponding to 2.715 Å. (b) Spot C corresponding to 2.715 Å. (c) Spot D corresponding to 2.715 Å, spot F corresponding to 1.400 Å, and spot E corresponding to 1.213 Å. (d) Spot G corresponding to 2.185 Å and spot H corresponding to 1.213 Å. The cross point in all images is the foot point; the black stripes are the dead areas of the detector. The full list of detected diffraction spots is presented in Table I.
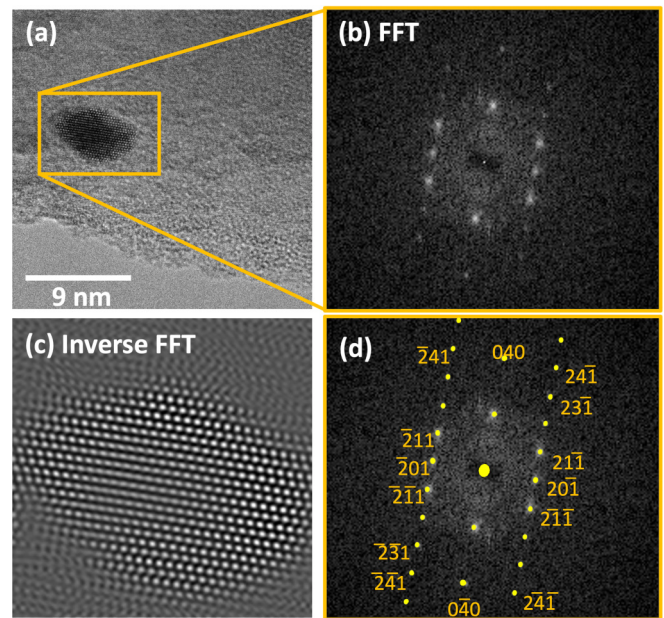

FIG. 5. Fast Fourier transform (FFT) analysis of nanoclusters. Example of analysis of high-resolution transmission electron microscopy (HRTEM) image of a nanocrystal in silicon sample irradiated at laser intensity 7.5×10^{19} W/cm^2. (a) HRTEM image of a nanocrystal in amorphous Si. (b) FFT analysis from the corresponding yellow-framed selected area in the HRTEM image shown in (a). (c) Inverse FFT image from (b), showing reconstruction of the nanocrystal. (d) Indexing with corresponding st12-Si crystal structure [9] (space group $P4_32_12$), overlaid on the FFT analysis shown in (b).

24 (22 phases), and 32 (100 phases) atoms per primitive cell [18].

Further study of such samples to assemble a full diffraction dataset is warranted to perform more quantitative structure data analysis. Nonetheless, the data clearly show that exotic Si phases, like those recovered from DAC [1,4–7,14], nanoindentation [7,8], and laser-induced transformations [10,11,16,17] can also be synthesized deep in the bulk of silicon crystal through laser irradiation at above relativistic intensity.

III. PHASE IDENTIFICATION IN SILICON NANOCRYSTALS

A. TEM analysis

HRTEM allows direct imaging of the individual atomic layers in the observed nanocrystals and subsequent identification of the crystal lattice structure through fast Fourier transform (FFT) analysis. It allowed phase identification within a notable number of nanocrystals with typical size in the range of 5–20 nm, see Figs. 5 and 6. Table II lists the interatomic distances and related crystal indices. It is instructive to note that the accuracy of interatomic distance determined by FFT analysis is about an order of magnitude lower than that determined from the XRD measurements above. The advantage of FTT imaging is in the visualization of the whole pattern, which is very useful for matching with schematic models of corresponding reciprocal space nodes.

During HRTEM analysis, we uncovered 59 nanocrystals of different size, quality, and scattering power. We performed FFT analysis on all these nanocrystals. Quite a number of those nanocrystals only showed 1 or 2 fully discernible reflections with only a small subset showing a full indexable pattern. We, therefore, present the overall resulting data in two ways. We first list all the measured d spacings and assign them to possible Si phases based on calculated d spacings, see Table II. We then show a select subset of HRTEM images and corresponding FFTs that give examples of fully indexable st12-Si, bt8-Si, and Si-VIII crystals, see Fig. 6. Note that we did not identify a fully indexable bc8-Si crystal within the nanocrystals analyzed.

FFT analysis of nanocrystals confirmed the presence of all crystal structures indicated by the XRD analysis. More HRTEM images and corresponding FFT analysis of interatomic distances with assigned silicon polymorphs are presented in Figs. S-03 and S-04 in Supplemental Material [46].

B. Energy-dispersive x-ray spectroscopy analysis of silicon purity

Finally, we also confirmed that all observed nanoparticles are indeed made of silicon. We performed spatially resolved energy-dispersive x-ray spectroscopy (EDX) elemental mapping analysis [54] of randomly selected areas in the TEM

TABLE II. FFT results. Analysis of HRTEM images of 59 nanocrystals showing the determined interatomic distances and related crystal structures of Si polymorphs. The first column shows the recovered d for the observed reflection with the corresponding accuracy. The last column indicates the number of clusters showing the corresponding interatomic spacing. The lattice parameters are given for a unit cell at 0 GPa pressure. Question marks indicate interatomic distances which cannot be identified with the known Si allotropes.

Identified Si crystal structures with space groups $d \pm \Delta d$ (Å)	Unassigned d (Å)	dc-Si $Fd\bar{3}m$ [52]	bc8-Si $Ia\bar{3}$ [4]	r8-Si $R\bar{3}$ [18]	st12-Si $P4_32_12$ [10]	bt8-Si $I4_1/a$ [10]	hd-Si $P6_3/mmc$ [15]	Si-VIII $P4_12_12$ [6]	No. reflection spots
Lattice parameters		$a = 5.4307$ Å	$a = 6.636$ Å	$a = 5.766$ Å, $\gamma = 109.47°$	$a = 5.678$ Å, $c = 6.825$ Å	$a = 6.676$ Å, $c = 6.522$ Å	$a = 3.80$ Å, $c = 6.28$ Å	$a = 8.627$ Å, $c = 7.500$ Å	
8.55 ± 1.02	??								1
5.20 ± 0.37	Si-IX [110] 5.29 Å[a]								4
4.71 ± 0.30			[110] 4.69 Å	[1−10], [100] 4.708 Å				[111] 4.732 Å	6
4.20 ± 0.23					[101] 4.36 Å, [010] 4.01 Å			[200] 4.31 Å	8
3.82 ± 0.20								[210] 3.858 Å[b]	5
3.60 ± 0.17	??								5
3.29 ± 0.14			[200] 3.32 Å	[11−1] 3.33 Å		[200] 3.33 Å	[100] 3.29 Å		12
3.13 ± 0.13[c]		[111] 3.135 Å[c]							29[c]
3.06 ± 0.12								[220] 3.05 Å[b]	13
2.90 ± 0.11					[012] 2.92 Å		[101] 2.91 Å		9
2.85 ± 0.10					[200] 2.84 Å			[202] 2.83 Å	5
2.73 ± 0.10			[211] 2.71 Å, [112] 2.68 Å	[110], [20−1] 2.72 Å		[211] 2.71 Å, [112] 2.68 Å		[310] 2.73 Å, [301] 2.68 Å	16
2.64 ± 0.09					[201] 2.62 Å, [112] 2.60 Å[b]				2
2.51 ± 0.08					[210] 2.54 Å			[003] 2.50 Å	5
2.42 ± 0.07					[221] 2.38 Å[b]				2
2.29 ± 0.07							[102] 2.27 Å	[302] 2.28 Å	9
2.21 ± 0.06					[022] 2.18 Å[b]				2
2.07 ± 0.05					[013] 2.11 Å	[301] 2.10 Å, [103] 2.06 Å			24

TABLE II. (Continued.)

Identified Si crystal structures with space groups $d \pm \Delta d$(Å)	Unassigned d(Å)	dc-Si $Fd-3m$ [52]	bc8-Si $Ia-3$ [4]	r8-Si $R-3$ [18]	st12-Si $P4_32_12$ [10]	bt8-Si $I4_1/a$ [10]	hd-Si $P6_3/mmc$ [15]	Si-VIII $P4_12_12$ [6]	No. reflection spots
2.00 ± 0.05					[220] 2.00 Å [113] 1.98 Å[b]				9
1.91 ± 0.05[c]		[220] 1.92 Å[c]		[11 − 3]1.92 Å[c]	[221] 1.92 Å[c]		[110] 1.90 Å[c]		22[c]
1.82 ± 0.04					[031] 1.82 Å			[412] 1.825 Å	20
1.77 ± 0.04			[312] 1.77 Å	[21 − 3], [10 − 3], [30 − 2], [210]1.78 Å	[310]1.79 Å [023]1.77 Å	[231] 1.78 Å [132] 1.77 Å [213] 1.75 Å	[103] 1.77 Å		4
1.71 ± 0.04				[22 − 2]1.66 Å	[311] 1.74 Å [004] 1.70 Å [032] 1.69 Å				7
1.63 ± 0.03[c]		[311] 1.6374 Å[c]				[004] 1.63 Å[c]	[112] 1.63 Å[c]		19[c]
1.55 ± 0.03[c]		[222] 1.569 Å[c]	[411] 1.56 Å[c]	[300] 1.57 Å[c]	[312] 1.58 Å [321] 1.53 Å[c]	[411] 1.57 Å [033] 1.55 Å [114] 1.54 Å[c]		[333] 1.58 Å [423] 1.53 Å[c]	30[c]
1.49 ± 0.03			[402] 1.48 Å				[202] 1.46 Å		3
1.42 ± 0.03			[332] 1.41 Å	[4 − 1 − 1], [220]1.42 Å	[322] 1.43 Å [133] 1.41 Å				2
1.36 ± 0.02[c]		[400] 1.3577 Å[c]				[422] 1.36 Å[c]			4[c]
1.31 ± 0.02			[413] 1.30 Å					[443] 1.30 Å	2
1.23 ± 0.02[c]		[331] 1.2459 Å[c]							9[c]
1.20 ± 0.02			[512] 1.21 Å				[114] 1.21 Å	[640] 1.20 Å	2
1.10 ± 0.02[c]		[422] 1.1085 Å[c]	[600] 1.10 Å[c]						2[c]
1.07 ± 0.01	??[b]								3
1.04 ± 0.01							[006] 1.05 Å[b]		6
0.93 ± 0.01								[901] 0.95 Å[b]	5

[a]Possible Si-IX, $P4_222$, [110] 5.29 Å.
[b]Uniquely identified interatomic distances at ambient pressure.
[c]Those reflections from dc-Si and possibly from other interatomic distances overlapping with dc-Si.
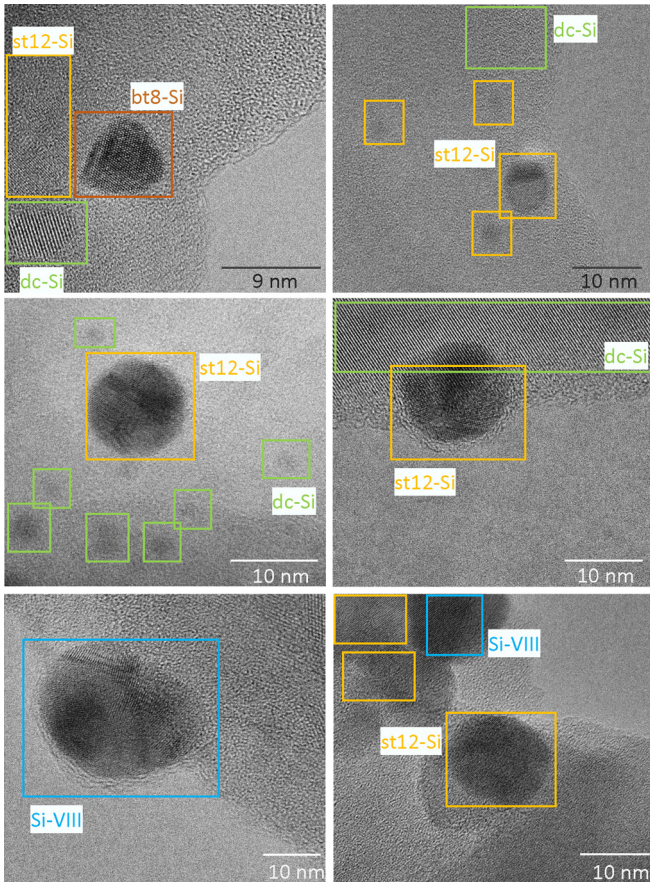
FIG. 6. High-resolution transmission electron microscopy (HRTEM) images of nanocrystals. Si polymorphs formed in the bulk of the sample irradiated at laser intensity 7.5×10^{19} W/cm^2. Fast Fourier transform (FFT) analysis of the selected areas reveals the presence of nanostructures of dc-Si indicated in green, st12-Si in yellow, Si-VIII in blue, and bt8-Si in red.
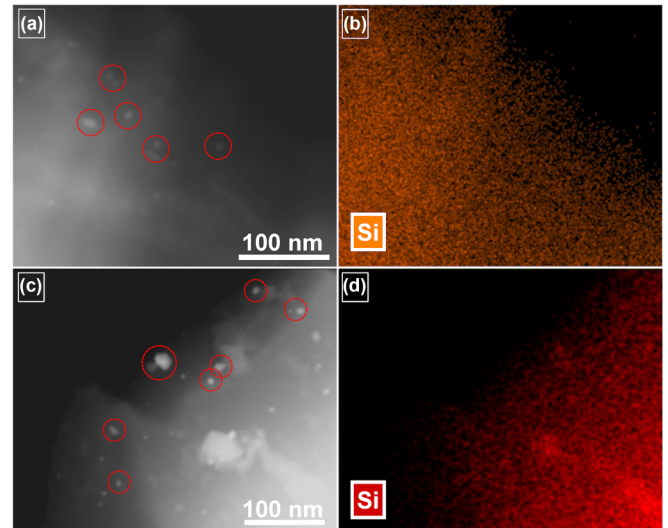

FIG. 7. High-angle annular dark-field (HAADF) scanning transmission electron microscopy (STEM) analysis. Images of (a) and (c) randomly selected areas and (b) and (d) corresponding spatially resolved energy-dispersive x-ray spectroscopy (EDX) Si chemical maps. The orange/red color in (b) and (d) corresponds to spatially resolved Si element. Si contrast remains the same in the presented images in (b) and (d); this confirms that the nanosized inclusions indicated by red circles in (a) and (c) consist purely of Si.

image, which gives precise elemental concentration at submicron resolution, see Fig. 7.

High-angle annular dark-field (HAADF) images were obtained using scanning TEM (STEM). These show the presence of nanocrystals with their size varying from ~5 to ~50 nm [Figs. 7(a) and 7(c)], while the elemental mapping in Figs. 7(b) and 7(d) demonstrates that Si is homogeneously distributed over the images. This confirms the observation of purely elemental silicon and the absence of any contamination. The absence of contamination is also supported by EDX spectra presented in Figs. S-05 and S-06 in Supplemental Material [46].

Furthermore, the HAADF image gives an indication of the quantity of nanocrystals within the amorphous matrix, suggesting that nanocrystals comprise up to 1% of the sample volume. The nanoscale size of the formed silicon polymorphs precluded us from a more accurate estimation of the volume of silicon converted into new structures under the laser pulse irradiation at above relativistic intensity. However, this serves as experimental proof that bulk conversion of silicon into a new structure is a feasible approach using relativistic intensities of laser radiation.

IV. DISCUSSION

The presented analysis of Raman spectra, XRD, and HRTEM images provides convincing evidence of the formation of pressure-induced exotic silicon polymorphs deep in the bulk of a silicon sample irradiated by a laser pulse at relativistic intensity. This includes the synthesis of intriguing phases not accessible by static techniques, specifically the st12 and bt8 structures, which have previously only been made by laser-induced microexplosions [7,10,11]. Especially st12-Si may thereby possess interesting band gap characteristics, as it is calculated to have an indirect gap of 1.1 eV within DFT and potential for superconductivity if doped. Given the typical underestimation of the gap within DFT, the gap is expected to be larger, likely larger than dc-Si, which would make this a technologically very intriguing phase of Si. Alternative methods for synthesis of this intriguing Si phase as presented here could eventually open avenues for the characterization of optical and electronic properties. In this paper, we thus present a considerable step forward in the restructuration of large volumes of such materials within a Si wafer by ultraintense and ultrashort laser pulses.

Post-mortem examination of the samples irradiated at the intensity above the relativistic threshold provides a basis for the semiquantitative analysis regarding the spreading of absorbed laser energy across the whole sample thickness by laser-generated energetic electrons. There are three major conclusions deduced from these experiments:

(1) Tightly focused ultrashort laser pulses at relativistic intensity produce ablated craters with the size two orders of magnitude larger than the laser focal spot size.

(2) The amount of ablated mass is the evidence that the large part of the pulse energy has been spent for the material

removal. On the other hand, the spallation at the rear surface of the 525-μm-thick Si sample is the indication of the deposition of significant energy density into the intact part of the target between the ablated and spalled craters. The MeV electrons generated at relativistic laser intensity have a stopping range in silicon comparable with the sample thickness [45]. Thus, it is likely that electrons deposited their energy across the whole thickness of the sample. A much slower ablation process at the front surface then followed. The recoil pressure of the ablated plasma drives the shock wave through the intact middle part of the sample. The shock wave arriving at the sample-vacuum interface then spalls off part of the material at the back of the sample.

(3) Formation of nanocrystals of at least six different high-pressure silicon polymorphs, including st12-Si and bt8-Si, in addition to the nanocrystals with original dc-Si structure, is observed across the thickness of the sample using Raman spectroscopy, XRD studies, and FFT analysis of the diffraction patterns from nanocrystal HRTEM images. Most of those nanocrystals are embedded in an amorphous silicon matrix created from the disordered silicon crystal lattice because of the absorbed MeV electron energy.

These observations serve as experimental proof that the original crystal structure was completely lost due to the ultraintense laser irradiation and ionization. We present below a self-consistent semiquantitative scenario based on the energy and mass conservation laws for the laser absorption, electron acceleration, material heating and ionization, and formation of the conditions for the observed crystal restructuring in the bulk.

A. Absorption of laser energy and ionization at relativistic laser intensity

The strength of the laser field expresses as the dimensionless amplitude of the laser electric field $a_0 = e\bar{A}/m_e c^2$, and the ponderomotive potential $p_{pm} = m_e c^2[(1 + a_0^2)^{1/2} - 1]$, where e is the electron charge, c is the speed of light, m_e is the electron mass, and $\bar{A}$ is the vector potential connected to the electric field amplitude $\bar{E}$ by the relation $\bar{E} = -\frac{1}{c}\frac{\partial \bar{A}}{\partial t}$ [55]. In practical units [28,50],

$$a_0 = \frac{e}{m_e c \omega}\left(\frac{8\pi I_l}{c}\right)^{1/2}$$
$$= \left(\frac{I_l \lambda^2}{1.375 \times 10^{18} \text{ [W μm}^2\text{/cm}^2\text{]}}\right)^{1/2}. \quad (1)$$

Here, ω is the laser frequency, I_l is the laser intensity in W/cm², and λ is in μm. For $\lambda = 800$ nm, the relativistic threshold $a_0 = 1$ is reached at the intensity level of $\sim 2.15 \times 10^{18}$ W/cm² [36,56]. At the highest intensity of 7.5×10^{19} W/cm² in our experiments, $a_0 = 5.91$, and thus, the interaction proceeds in the ultrarelativistic regime.

The ultrarelativistic laser pulse, obliquely incident at 53.4° to the target normal linearly polarized in the plane of incidence (*p*-polarized), ionizes the sample by the over-the-barrier ionization mechanism, allegedly stripping all of 14 electrons from Si atom. The total ionization losses of 4.66 keV per atom during the pulse are much less than the energy of the laser-generated electrons.

B. Energy of electrons in the absorption zone

The laser pulse penetrates the solid to the depth of c/ω_{pe}, where ω_{pe} is the electron plasma frequency for the relativistic case. The trajectory of electrons in a strong linearly polarized field at relativistic intensity has a figure-of-eight shape. The longitudinal displacement is proportional to the magnetic force $[e \times (v \times B)]/c \propto a_0$; $(v \propto a_0)$, which is proportional to a_0^2, whereas the transverse displacement along the electric field scales up with a_0. Therefore, at $a_0 > 1$, the longitudinal momentum becomes much larger than the transverse one, and the electrons are accelerating along the k vector of the wave.

Strong repulsion between electrons and the nonlinear relativistic effects creates very complicated electronic orbits, which enhance laser absorption even within a single optical cycle [57–60]. The magnetic force $(v \times B)$ acts on the electrons swiftly, accelerating them in the direction of the laser beam. Due to the oblique incidence, this force has two components, along the surface of the sample and perpendicular to the surface, making the trajectories of the electrons rather complicated. The electron motion is the source of the relativistic nonlinear effects [57,59], and the nonlinearity of the electron orbits enhances the laser-matter interaction. The electron orbits exhibit remarkable chaos within a single optical cycle. This strong orbital nonlinearity is responsible for the efficient absorption of the laser energy in a few optical cycles. In the case considered here, the 25 fs pulse duration equals ~ 10 optical cycles ($2\pi/\omega = 2.66$ fs). The main absorption mechanism is apparently plasma heating by the oscillating component of the pondermotive force of intense laser light, the $j \times B$ heating [59–61]. The conversion efficiency of laser energy to electrons increases with laser intensity from ~ 20 to 30% at the relativistic intensity up to 80% at a 10 times higher level [37,59,61].

The electron energy can be approximated by Boltzmann distribution for a major part of electrons temperature kT_e with a high-energy tail kT_h that is of the order of the ponderomotive potential [36,37,62]:

$$kT_h[\text{MeV}] \cong p_{pm} = m_e c^2(\gamma - 1)$$
$$= 0.511 \times \left[(1 + a_0^2)^{1/2} - 1\right], \quad (2)$$

where k is the Boltzmann constant, and $\gamma = (1 - v_e^2/c^2)^{-1/2}$ is the relativistic Lorentz factor. At the highest laser intensity in our experiments, the electron temperature is $kT_e \sim 0.1 - 0.3$ MeV, and the energy of the high-energy tail based on the ponderomotive potential scale law is $kT_h \cong 2.56$ MeV. The fraction of the incident laser energy absorbed into the hot electrons forward-propagating into a solid sample is $\sim 10–20\%$ [38,59].

The high-energy tail of hot electrons, with energy from MeV and higher, penetrates the solid during the laser pulse and distributes the absorbed laser energy into a volume much larger than that limited by the spot size on the surface and the skin layer depth into the target [39].

Santala *et al.* [63] found that, for shallow plasma density gradients, the fast electron angular distribution becomes random. The authors suggested that $j \times B$ heating in the long-scale plasma supports this observation. According to the particle-in-cell calculations from Ref. [63] at the intensity

10^{20} W/cm^2, the additional electron beam is generated in the direction of the obliquely incident laser beam propagation. The conditions in our experiments and calculations are reasonably like those in Ref. [63]. Therefore, the shallow plasma gradients along with the orbital nonlinearities contribute to the almost isotropic angular distribution of electron trajectories within the target. That was the reason for the ablated volume being much larger, about two orders of magnitude larger than the laser-target interaction zone of the focal spot.

In these conditions, the ponderomotive scaling significantly exaggerates the temperature of the hot electrons. The scaling and discussion in Mordovanakis *et al.* [64] suggest that, at the ultrarelativistic intensity, the temperature of the hot electrons scales as $kT_h \propto [I_{18}\lambda_\mu^2]^\alpha$, where $\alpha = 0.33$–0.64, and I_{18} is intensity in units of 10^{18} W/cm^2. The results of our experiments suggest the following scaling for hot electrons in the considered case:

(1) at $a_0 > 1.0$, $kT_h \approx 118(\mp 5) \times [I_{18}\lambda_\mu^2]^{0.64\mp 0.05}$ keV; for $I_{18} = 75$ and $\lambda = 0.8$ μm, $kT_h = 1.56$ MeV;

(2) at $a_0 \gg 1$, $kT_h \approx 290 \times [I_{18}\lambda_\mu^2]^{1/3}$ keV; for $I_{18} = 75$ and $\lambda = 0.8$ μm, $kT_h = 1.054$ MeV.

Summing up the above analysis of the energy of electrons, we can conclude that the energy distribution of the electrons entering from the absorption zone into the solid sample can be characterized by two temperatures. A major part of the electrons has temperature of 0.1–0.3 MeV, while a relatively small part of the electrons in the high-energy tail has energy of ~ 1 MeV. The angular distribution of electron trajectories inside the bulk of the sample, and especially in the part remaining intact, is apparently isotropic. The isochoric heating of the solid by the fast electrons is accompanied by a much slower shock wave created by the electronic pressure gradient [65].

C. Spreading of energy of the relativistic electron over the target volume

The indication of the strong collective effects related to the very high density of the relativistic electrons follows from the estimates for the current created during the pulse, assuming the current is forward directed into the silicon bulk. The electron bunch emerged from the laser-target interaction volume of the focal spot carries the enormous current $J_{\exp} = en_e v_e S_{\text{foc}} \cong e\frac{I_{\text{las}}}{\varepsilon_e} S_{\text{foc}} \cong 9.6$ MA (here, n_e, v_e, and ε_e are the electron density, speed, and energy, correspondingly). Taking the speed $v_e = 0.98c$ at $\varepsilon_e = 2.56$ MeV, $J_{\exp} \cong 9.6$ MA, which is several orders of magnitude above the Alfven current limit [66].

Alfven [66] demonstrated that, at a certain current value, the direct current is impossible because the trajectories of the electrons became entangled due to the influence of the self-generated magnetic field. It is easy to see that Alfven's limit for the current of the electrons is set by the repulsion of the electrons. Indeed, the distance of the closest approach $r_{\min}$ for the electrons possessing kinetic energy ε_e is $r_{\min} \approx e^2/\varepsilon_e$. Taking this distance as a linear and transverse scale for the current, one gets $J = en_e v_e \pi r^2 \approx e v_e/r_{\min}$. Therefore, the maximum possible current is the Alfven current limit $J_{\text{Alf}} = v_e \varepsilon_e/e \approx \gamma \beta m_e c^3/e$, where $\beta = v_e/c$ [60]. For the 2.56 MeV electrons [$\beta = 0.98$, $\gamma = (1 - \beta^2)^{-1/2} = 5$], the Alfven current limit is

$J_{\text{Alf}} \cong 420$ kA. This is the reason for the bunch of relativistic electrons to deposit their energy by spreading it over a large volume around the focal spot and across the whole thickness of the silicon target.

The presented estimates serve as an indication that the self-generated magnetic field has a strong effect on the orbits of the electrons, resulting in filamentation, branching, and very fast diverging of the propagation of the electrons. The large area of the ablation crater, which is about two orders of magnitude wider than the focal spot at the highest intensity, is evidence of a fast spreading of the flow of electrons in the silicon target.

The above consideration also serves as the indication that plasma instabilities dominate the propagation of the electrons inside the solid. A single energetic particle passing through a solid loses its energy on the excitation and ionization of atomic electrons. The Fourier component of the particle field with the wave vector k transfers to an electron a momentum $\hbar k$. Many atoms and atomic electrons are involved in this process by creating a large negative real part of the dielectric function in the excited medium, which is the polarization of the medium from the classical viewpoint [67]. The electric field E acts on a particle with the stopping force $F_{\text{stop}} = eE$, in the direction opposite to the velocity of a particle. This field might be associated with the return current of slow electrons compensating the direct current of the fast particle [68]. The work produced by this force is the energy loss of a particle. The stopping range in a solid where the electron loses its energy ε_e estimates as $l_{\text{stop}} \approx \frac{\varepsilon_e}{F_{\text{stop}}}$. It is essential that both relativistic and nonrelativistic stopping forces are identical to the quantum mechanical stopping force induced by the Coulomb scattering. For the fast nonrelativistic electrons, the binary Coulomb collisions dominate the energy transfer from the electrons to the ions $F_{\text{stop}}^{\text{nonrel}} \propto \frac{2\pi n_e e^4}{m_e v_e^2}$.

The return current excites the electromagnetic Weibel-like instability. The growth rate of this instability estimates as $\sim \omega_{pe} v_e/c$. Here, ω_{pe} is the plasma frequency corresponding to the number density of plasma electrons and the velocity of slow electrons. The strong return current develops in <1 ps. The electric field associated with the return current generates the magnetic field in accordance with Faraday's law with a growth rate of ~ 100 Tesla/ps [60]. The electron bunch entering a solid from the absorption zone quickly becomes divergent, splits into filaments, and transforms into a broad cone.

D. Silicon restructuring

The energy of the 25-fs-short ultrarelativistic pulse has been transformed into a bunch of energetic electrons in the focal volume of a few cubic microns. Finally, the absorbed laser energy has been spread by fast electrons unevenly over the sample thickness, with most of the energy spent on ablation. The simplest estimate of the average energy density created by 0.6 J of laser pulse energy spread over the volume of a hemisphere with a radius of 200 μm ($V = 1.67 \times 10^{-5}$ cm^3) gives ~ 36 GPa pressure. The observed polymorphs of Si formed from metallic β-Sn Si at above ~ 12 GPa [7]. Assuming the uneven energy distribution, one can reasonably suggest that the resulting delivery of energy density by the shock wave is in the range of a few tens of GPa. The shock-wave pressure

is well below the Young's modulus of Si, which is within the range 131–170 GPa [69], coupled with the heating from the energetic electrons.

The combined action of MeV electrons and the pressure of the shock wave move the ionized atoms from their equilibrium positions of the silicon crystal lattice and partially reconstruct into the different atomic arrangements in the process of fast quenching and recombination as well as freezing a significant part in a disordered state. The branched propagation, in addition to the recoil pressure, allows for the formation of the observed high-pressure Si phases deep in the target bulk. The fact that about half of the original sample thickness between the beds of the ablated and spalled craters remained in one piece indicates that the energy density delivered to the middle part of the target thickness has been less than Young's modulus of Si.

Ablation of $\frac{1}{3}$ of the target thickness creates significant recoil pressure at the bottom of the ablated volume. This pressure drives the shock wave through the intact part of the target. The pressure at the shock front decreases during the propagation approximately inverse to the cubic root of the distance. Therefore, an estimate of the ablated ion energy (velocity) can be made by dividing the laser energy per number of ablated atoms found from the measurements of ablated volume. To ablate material, the energy per atom equal to the cohesion energy plus the kinetic energy for the ion removal should be delivered. It appears that, for the most intense pulse of 0.6 J, the kinetic energy equals a few eV per ion (ablated Si ion velocity is $\sim 10^6$ cm/s). Therefore, the recoil pressure at the bottom of the ablated volume equals a few hundred GPa. At the back surface, it reduces to $\sim$100 GPa capable of producing spallation observed in the experiment. Note that this is clear evidence of the existence of a few hundred GPa pressure in the middle of intact target, which is enough for the observed phase transformations. Similar estimates for the 10 times less energy per pulse produce the energy at the rear surface <10 GPa, which is not sufficient for spallation in accord with the measurements.

Let us now evaluate the current results from the point of conversion efficiency into new structures and compare with the results of our previous experiments [10]. There is a difference of six orders of magnitude in single pulse laser energy of up to 0.6 J in the current experimental conditions when compared with 0.1–1.0 μJ in our previous experiments, which signifies the difference in the laser-matter interaction physical processes. Analysis of TEM images of the embedded nanoparticles (Figs. 6 and 7 and Figs. S-05(a) and S-05(d) in the Supplemental Material [46]), supported by the intensity signatures in XRD analyses (Figs. 3 and 4), suggests that up to 1% of silicon mass was converted into the new crystal structures. To estimate the converted mass, we consider the experiment with the highest laser intensity of 7.5×10^{19} W/cm^2 (0.62 J per single pulse). The affected volume of silicon of 1.67×10^{-5}cm^3 comprises $\sim 3.9 \times 10^{-5}$ g of the affected mass, see Fig. 1 above and Fig. S-02 and Table S-01 in Supplemental Material [46]. The estimated 1% of the converted mass gives $\sim 3.9 \times 10^{-7}$ g of new silicon structures formed with 0.62 J laser pulse, or $\sim 6 \times 10^{-7}$ g of converted mass per Joule of laser energy. Similar evaluation for our previous experimental conditions [10] of $\sim 10^{-14}$ g new phases with

<1 μJ corresponds to 10^{-8} g per Joule. This is about a two orders of magnitude increase in the efficiency that correlates well with the very similar about two orders of magnitude increase in the ablated silicon volume clearly seen as soon as the laser intensity passes the relativistic intensity threshold at $\sim 2 \times 10^{18}$ W/cm^2, see Fig. 1(h) and Fig. S-02 and Table S-01 in Supplemental Material [46].

We conclude that the observed silicon polymorphs were generated at the high-energy density (i.e., pressure) created in the bulk silicon by MeV electrons plus the recoil-pressure-driven shock wave, followed by the rapid depressurization and thermal quenching. These uncommon tetrahedral Si phases may result from a final transformation from metallic states of Si, like those known to form at very high pressures [1–6] in static conditions. Material transformation under rapid quenching from denser metallic phases may result in alternative restructuring pathways and the formation of metastable tetragonal phases that are not possible under equilibrium conditions typical for a DAC or by nanoindentation methods.

V. CONCLUSIONS AND OUTLOOK

In summary, by using laser pulses at relativistic intensity, we have produced metastable tetragonal phases of Si within the bulk of the material. The possibly decent amount of these phases created here may open avenues to allow their further study using various spectroscopic and imaging techniques as well as eventually even electric probes. The high-energy-density conditions are generated inside the intact part of the sample by the flux of MeV electrons ionized the bulk of the sample and by the following shock wave driven by the recoil pressure of the large amount of ablated material. These conditions led to the rearrangement of the silicon matrix into at least six different polymorphs. The *ex situ* studies of the remaining intact part of the sample were performed using micro-Raman, synchrotron XRD, and HRTEM. The XRD and HRTEM analyses of recovered nanocrystals revealed that these inclusions were formed by known Si phases such as bc8, r8, st12, bt8, hd-Si, and Si-VIII along with dc-Si nanocrystals. This is particularly encouraging for the cases of st12-Si and bt8-Si, which cannot be made by static pressure techniques and where there is no other method to scale up their volumes. The structural analysis shows the exotic Si phases created in the form of nanocrystalline clusters 5–20 nm in size, pointing to the structure formation near the track of the energetic electrons. Randomly selected TEM images indicate that up to $\sim$1% of silicon bulk between the ablated and spalled craters is converted into such crystalline nanoparticles. The evaluated increase of the converted silicon mass when compared with previous results obtained at well below the relativistic intensity threshold [10] correlates well with the significant increase in the ablated mass at the intensities above the threshold.

Such exotic metastable phases of Si are expected to be greatly advantageous since they enable simple pressure-induced band gap engineering for innovative future applications. For example, the known narrow-band-gap r8 polymorph is predicted to possess a significantly larger light absorption overlap with the infrared solar spectrum than standard dc-Si [19]. Interestingly, st12-Si may possess a relatively

large band gap 1.1 eV, may become superconducting if sufficiently doped, and may exhibit thermal stability, potentially >500 °C [35,70]. Indeed, several further Si structures with (quasi-)direct band gaps for future photovoltaic devices and other useful electronic properties have been predicted, e.g., see Ref. [7] and references therein.

Further experimental and theoretical studies are needed to identify the range of pressures that can be generated in a solid part of the intact sample and of the methods needed to fully control the conditions inside the bulk [70]. This could be achieved, for example, by the interaction of the ultrarelativistic, ultrashort ($10^{19} - 10^{20}$ W/cm^2, <100 fs) high-energy-contrast laser pulse [71–75] with the silicon targets with varied thickness [71].

Finally, the method of formation of exotic phases deep inside the bulk by irradiation of silicon by ultraintense and ultrashort laser pulses is applicable to a wide range of materials, not just to silicon. The unexplored domain of material transformations exposed to a high flux of laser-produced MeV electrons opens pathways for the conversion into new crystal structures applicable to a wide range of materials in considerably larger volumes, all preserved for further studies and exploitation. We thus expect that laser pulses at relativistic intensity will open a fruitful roadmap toward material discoveries and applications.

APPENDIX: METHODOLOGY

1. Ultraintense ultrashort laser irradiation conditions

A 40 TW Ti : sapphire laser system with a double-chirped pulse amplification (CPA) configuration (Pulsar, Amplitude Technology Co.) was used in the experiments. The laser pulses generated at 800 nm wavelength were amplified by using the CPA technique [57]. A pair of gratings was used to compress the laser pulse down to 25 fs at FWHM level. The pulse duration was measured by self-referenced spectral interferometry (Wizzler by Fastlight). The frontend laser system adapted a double CPA layout with crossed polarized rotation to suppress amplified spontaneous emission (ASE) intensity [72,73]. The intensity contrast ratio was determined by a third-order cross-correlation (Sequoia by Amplitude Tech.). Laser pulses with up to ∼1 J energy were generated in the experiments. The root mean square (RMS) stability of the laser energy was 2%. The averaged energy contrast, i.e., the energy ratio of the ASE in the temporal range between −70 and −20 ps before the pulse peak to the main peak power, was measured to be 7.7×10^{-10}, providing assurance of the absence of any surface modification before the arrival of the 25 fs pulse, see Sec. S-I in Supplemental Material [46].

Single linearly polarized 25 fs pulses were tightly focused on the surface of Si samples using an off-axis parabolic mirror with a reflected focal length of 165 mm, off-axis angle of 32.5 °, and f number 3.7 (NA = 0.135). The elliptically shaped focal spot of 14 × 3 μm at FWHM energy level was formed at the angle of incidence of ∼36.6 ° to the crystal surface, which corresponds to surface area $S_{foc} = 3.3 \times 10^{-7}$ cm^2. The incidence angle was chosen to increase the absorption of *p*-polarized laser light by resonance absorption mechanism. A laser intensity of up to 7.5×10^{19} W/cm^2 was reached at the maximal pulse energy of 0.62 J, which corresponds to a laser fluence of 1.87 MJ/cm^2 on the sample surface.

2. Silicon crystal sample

The laser irradiated samples were boron-doped, 525-μm-thick high-purity dc-Si <100> crystals with electrical resistivity 1–20 Ohm cm, so that the dopant concentration was of the order of ∼ 10^{-11} for an indirect band gap of 1.12 eV

at room temperature [77]. Square-shaped 4×4 mm^2 silicon samples were mounted on a stainless-steel holder on top of the holes of 4 mm in diameter, so that the back of the sample was in free space during the experiments.

The ablated volumes on the Si surface were characterized by a three-dimensional laser scanning confocal microscope (Keyence VK-9710) based on a 408 nm laser source, see details in Sec. S-II in the Supplemental Material [46].

3. Raman microspectroscopy

Raman characterization of the bulk of the sample between the ablated and spalled craters was performed with a Renishaw InVia Reflex Raman spectrometer in confocal geometry. Spectra were obtained with 532 and 633 nm lasers using ×20, 0.25 NA (Olympus SLMPLN 20X), where a large depth of field provided more leniency in the focus of the Raman laser across the rough surfaces. Approximately 20 Raman maps and 30 linescans were used to investigate the samples. Raman spectra were collected on a Peltier-cooled charge-coupled device detector with 1200 and 2400 lines/mm gratings. The relative precision of locating peaks was within 0.1–0.5 cm^{-1}, where the variation is dependent on the peak strength relative to any overlapping peaks. Analysis was performed using the Wires 4 software package.

4. X-ray microdiffraction analysis with Cu-Kα radiation

The 2D patterns of x-ray microdiffraction of the affected area of the sample were measured using a Rigaku SmartLab diffractometer under Cu-$K\alpha$ radiation at 1.54 Å (40 kV, 40 mA). A CBO-f Poly-capillary was used to converge parallel line focus beam to a point focus, tailored by a 0.5 mm height-limiting slit and a 0.5 mm incident slit. A Hypix3000 detector was used in 2D scanning mode 121.7 mm away from the sample. The sample area was aligned on a Chi-Phi cradle stage, both drives of which were continuously oscillating during data collection to randomize crystal orientations experimentally. The 2D XRD pattern from $10°$ to $90°$ 2θ was integrated into 1D data at a step size $0.01°$ 2θ/step using Rigaku 2DP v2.1.6 software, followed by the phase identification against ICDD PDF-4+ database in Diffrac.EVA v5 software.

5. Synchrotron XRD with 30 keV radiation

XRD was performed in the endstation of the BL22XU Beamline in SPring8. The x-ray beam of $\varepsilon \pm \Delta\varepsilon = 30.047 \pm 0.048$ keV was shaped to a 50 μm square by two slits located upstream of the sample. The first slit limited the beam aperture, and the second slit cut the scattered x-ray from the first slit to prevent stray x rays on the sample. The x ray was irradiated to the rear side of the sample (here, front side is the crater side), and the crater center was placed on the center of the x-ray beam.

The transmitted x ray was detected by an x-ray 0D detector, and the sample was positioned at the maximum x-ray transmittance; the accuracy of the location in the crater was 50 μm. A beam stop was placed behind the sample to stop the transmitted x ray. A 2D x-ray detector (PILATUS3 R 300K by DECTRIS) was used to detect diffracted x ray from the sample. The camera was fixed at the location such that the camera length (distance between the sample and the camera detection plane) of 254.14 ± 0.2 mm and the angle of $2\theta_0$ of $17.5°$. The x-ray incidence angle to the sample was varied by two rotation stages (ϕ, ω angles). Two experimental runs were performed. In the first run, the angle ϕ was varied from $-10°$ to $+10°$ with a step of $5°$, and the angle ω was varied from $-5°$ to $+5°$ with a step of $0.1°$. In the second run, the angle ϕ was fixed at $15°$, and the angle ω was varied from $1.5°$ to $2.5°$ with a step of $0.1°$. The sample was exposed for 100 s at each set of angles (ϕ, ω).

The experimental error ranges in the interatomic distance measurements in Table I were evaluated considering the accuracy of measurement of the diffraction angles (ϕ, ω), the accuracy of measured distance from the Si sample to the detector of 0.2 mm, the width of the x-ray energy peak $\Delta\varepsilon$ = 0.048 keV, and the size of pixels in the detector, which was 0.172×0.172 μm^2.

6. HRTEM

The atomic structure of the samples was studied by HRTEM, selected area electron diffraction and HAADF-STEM imaging combined with EDX mapping, all with a 200 kV JEM-2100 JEOL microscope equipped with an energy-dispersive x-ray spectrometer (Oxford Instruments). Samples for TEM analysis were prepared by grinding small pieces of a Si wafer from the exposed area in an agate mortar under ethanol. After grinding, the ethanol suspension was applied to a TEM copper grid.

---

[1] A. Mujica, A. Rubio, A. Muñoz, and R. J. Needs, High-pressure phases of group-IV, III–V, and II–VI compounds, Rev. Mod. Phys. **75**, 863 (2003).

[2] J. C. Jamieson, Crystal structures at high pressures of metallic modifications of silicon and germanium, Science **139**, 762 (1963).

[3] P. F. McMillan, Pressing on: The legacy of Percy W. Bridgman, Nat. Mater. **4**, 715 (2005).

[4] J. S. Kasper and S. M. Richards, The crystal structures of new forms of silicon and germanium, Acta Cryst. **17**, 752 (1964).

[5] L. Zhang, Y. Wang, J. Lv, and Y. Ma, Materials discovery at high pressure, Nat. Rev. Mater. **2**, 17005 (2017).

[6] Y-X. Zhao, F. Buehler, J. R. Sites, and I. L. Spain, New metastable phases of silicon, Solid State Commun. **59**, 679 (1986).

[7] B. Haberl, T. A. Strobel, and J. E. Bradby, Pathways to exotic metastable silicon allotropes, Appl. Phys. Rev. **3**, 040808 (2016).

[8] S. Wong, B. Haberl, B. C. Johnson, A. Mujica, M. Guthrie, J. C. McCallum, J. S. Williams, and J. E. Bradby, Formation

of an r8-dominant Si material, Phys. Rev. Lett. **122**, 105701 (2019).

[9] D. Y. Kim, S. Stefanoski, O. O. Kurakevych, and T. A. Strobel, Synthesis of an open-framework allotrope of silicon, Nat. Mater. **14**, 169 (2015).

[10] L. Rapp, B. Haberl, C. J. Pickard, J. E. Bradby, E. G. Gamaly, J. S. Williams, and A. V. Rode, Experimental evidence of new tetragonal polymorphs of silicon formed through ultrafast-laser-induced confined microexplosion, Nat. Commun. **6**, 7555 (2015).

[11] L. A. Smillie, M. Niihori, L. Rapp, B. Haberl, J. S. Williams, J. E. Bradby, C. J. Pickard, and A. V. Rode, Exotic silicon phases synthesised through ultrashort laser-induced microexpolsion: Characterisation with Raman microspectroscopy, Phys. Rev. Mater. **4**, 093803 (2020).

[12] E. J. Davies, P. J. Carter, S. Root, R. G. Kraus, D. K. Spaulding, S. T. Stewart, and S. B. Jacobsen, Silicate melting and vaporization during rocky planet formation, J. Geophys. Res. Planets **125**, e2019JE006227 (2020).

[13] J. E. Chambers, Making more terrestrial planets, Icarus **152**, 205 (2001).

[14] R. O. Piltz, J. R. Maclean, S. J. Clark, G. J. Ackland, P. D. Hatton, and J. Crain, Structure and properties of silicon XII: A complex tetrahedrally bonded phase, Phys. Rev. B **52**, 4072 (1995).

[15] J. S. Kasper and R. H. Wentorf, Hexagonal (wurtzite) silicon, Science **197**, 599 (1977).

[16] M. J. Smith, Y. T. Lin, M-J. Sher, M. T. Winkler, E. Mazur, and S. Gradečak, Pressure-induced phase transformations during femtosecond-laser doping of silicon, J. Appl. Phys. **110**, 053524 (2011).

[17] M. Tsujino, T. Sano, O. Sakata, N. Ozaki, S. Kimura, S. Takeda, M. Okoshi, N. Inoue, R. Kodama, K. F. Kobayashi *et al.*, Synthesis of submicron metastable phase of silicon using femtosecond laser-driven shock wave, J. Appl. Phys. **110**, 126103 (2011).

[18] V. E. Dmitrienko and V. A. Chizhikov, An infinite family of bc8-like metastable phases in silicon, Phys. Rev. B **101**, 245203 (2020).

[19] B. D. Malone, J. D. Sau, and M. L. Cohen, *Ab initio* study of the optical properties of Si-XII, Phys. Rev. B **78**, 161202(R) (2008).

[20] J. M. Besson, E. H. Mokhtari, J. Gonzalez, and G. Weill, Electrical properties of semimetallic silicon III and semiconductive silicon IV at ambient pressure, Phys. Rev. Lett. **59**, 473 (1987).

[21] H. Zhang, H. Liu, K. Wei, O. O. Kurakevych, Y. L. Godec, Z. Liu, J. Martin, M. Guerrette, G. S. Nolas, and T. A. Strobel, BC8 silicon (Si-III) is a narrow-gap semiconductor, Phys. Rev. Lett. **118**, 146601 (2017).

[22] B. J. Henderson, M. C. Marshall, T. R. Boehly, R. Paul, C. A. McCoy, S. X. Hu, D. N. Polsin, L. E. Crandall, M. F. Huff, D. A. Chin *et al.*, Shock-compressed silicon: Hugoniot and sound speed up to 2100 GPa, Phys. Rev. B **103**, 094115 (2021).

[23] M. Guerette, M. D. Ward, L. Zhu, and T. A. Strobel, Single-crystal synthesis and properties of the open-framework allotrope Si_{24}, J. Phys.: Condens. Matter **32**, 194001 (2020).

[24] T. B. Shiell, L. Zhu, B. A. Cook, J. E. Bradby, D. G. McCulloch, and T. A. Strobel, Bulk crystalline 4*H*-silicon through a metastable allotropic transition, Phys. Rev. Lett. **126**, 215701 (2021).

[25] S. Pandolfi, C. Renero-Lecuna, Y. Le Godec, B. Baptiste, N. Menguy, M. Lazzeri, C. Gervais, K. Spektor, W. A. Crichton, and O. O. Kurakevych, Nature of hexagonal silicon forming via high-pressure synthesis: Nanostructured hexagonal 4*H* polytype, Nano Lett. **18**, 5989 (2018).

[26] C. Lin, X. Liu, D. Yang, X. Li, J. S. Smith, B. Wang, H. Dong, S. Li, W. Yang, and J. S. Tse, Temperature- and rate-dependent pathways in formation of metastable silicon phases under rapid decompression, Phys. Rev. Lett. **125**, 155702 (2020).

[27] S. Pandolfi, S. B. Brown, P. G. Stubley, A. Higginbotham, C. A. Bolme, H. J. Lee, B. Nagler, E. Galtier, R. L. Sandberg, W. Yang *et al.*, Atomistic deformation mechanism of silicon under laser-driven shock compression, Nat. Commun. **13**, 5535 (2022).

[28] S. Juodkazis, K. Nishimura, S. Tanaka, H. Misawa, E. G. Gamaly, B. Luther-Davies, L. Hallo, P. Nicolai, and V. T. Tikhonchuk, Laser-induced microexplosion confined in the bulk of a sapphire crystal: Evidence of multimegabar pressures, Phys. Rev. Lett. **96**, 166101 (2006).

[29] E. G. Gamaly, S. Juodkazis, K. Nishimura, H. Misawa, B. Luther-Davies, L. Hallo, P. Nicolai, and V. T. Tikhonchuk, Laser-matter interaction in a bulk of a transparent solid: Confined microexplosion and void formation, Phys. Rev. B **73**, 214101 (2006).

[30] E. G. Gamaly, L. Rapp, V. Roppo, S. Juodkazis, and A. V. Rode, Generation of high energy density by fs-laser induced confined microexplosion, New J. Phys. **15**, 025018 (2013).

[31] E. G. Gamaly, S. Juodkazis, and A. V. Rode, Extreme energy density confined inside a transparent crystal: Status and perspectives of solid-plasma-solid transformations, Nanomaterials **8**, 555 (2018).

[32] E. G. Gamaly and A. V. Rode, Physics of ultra-short laser interaction with matter: From phonon excitation to ultimate transformations, Prog. Quantum Electron. **37**, 215 (2013).

[33] R. P. Drake, High-energy-density physics, Phys. Today **63**(6), 28 (2010).

[34] C. J. Pickard and R. J. Needs, *Ab initio* random structure searching, J. Phys.: Condens. Matter **23**, 053201 (2011).

[35] B. D. Malone, J. D. Sau, and M. L. Cohen, *Ab initio* survey of the electronic structure of tetrahedrally bonded phases of silicon, Phys. Rev. B **78**, 035210 (2008).

[36] R. P. Drake, *High-Energy-Density Physics: Foundation of Inertial Fusion and Experimental Astrophysics*, 2nd ed. (Springer, Cham, 2018).

[37] S. C. Wilks, W. L. Kruer, M. Tabak, and A. B. Langdon, Absorption of ultra-intense laser pulses, Phys. Rev. Lett. **69**, 1383 (1992).

[38] N. F. Beier, H. Allison, P. Efthimion, K. A. Flippo, L. Gao, S. B. Hansen, K. Hill, R. Hollinger, M. Logantha, Y. Musthafa *et al.*, Homogeneous, micron-scale high-energy-density matter generated by relativistic laser-solid interactions, Phys. Rev. Lett. **129**, 135001 (2022).

[39] D. Umstadter, Relativistic laser-plasma interactions, J. Phys. D: Appl. Phys. **36**, R151 (2003).

[40] M. A. Topinka, B. J. LeRoy, R. M. Westervelt, S. E. J. Shaw, R. Fleischmann, E. J. Heller, K. D. Maranowski, and A. C. Gossard, Coherent branched flow in a two-dimensional electron gas, Nature (London) **410**, 183 (2001).

[41] A. Daza, E. J. Heller, A. M. Graf, and E. Räsänen, Propagation of waves in high Brillouin zones: Chaotic branched flow and stable superwires, Proc. Natl. Acad. Sci. USA **118**, e2110285118 (2021).

[42] E. J. Heller, R. Fleischmann, and T. Kramer, Branched flow, Phys. Today **74**(12), 44 (2021).

[43] Yu. A. Il'insky and L. V. Keldysh, *Electromagnetic Response of Material Media* (Plenum Press, New York, 1994).

[44] E. G. Gamaly, A. V. Rode, B. Luther-Davies, and V. T. Tikhonchuk, Ablation of solids by femtosecond lasers: Ablation mechanism and ablation thresholds for metals and dielectrics, Phys. Plasmas **9**, 949 (2002).

[45] Stopping-power and range tables for electrons, protons, and helium ions, NIST Standard Reference Database 124, (2017); https://physics.nist.gov/PhysRefData/Star/Text/intro.html.

[46] See Supplemental Material at http://link.aps.org/supplemental/10.1103/PhysRevResearch.6.023101 for laser pulse intensity contrast (S-I); characterization of ablated craters (S-II); FFT analysis of HRTEM images (S-III); high-angle annular dark-field (HAADF) images and EDX spectra (S-IV); and stopping power of electrons in Si (S-V).

[47] L. Rapp, T. Matsuoka, K. L. Firestein, D. Sagae, H. Habara, K. Mukai, K. A. Tanaka, E. Gamaly, R. Kodama, Y. Seto *et al.*, Search for high-pressure silicon phases: Reaching the extreme conditions with high-intensity laser irradiation, in *Ultrafast Laser Nanostructuring*, edited by R. Stoyan and J. Bonse, Springer Series in Optical Sciences, Vol. 239 (Springer, Cham, 2023), Chap. 13, pp. 471–494.

[48] B. C. Johnson, B. Haberl, J. E. Bradby, J. C. McCallum, and J. S. Williams, Temperature dependence of Raman scattering from the high-pressure phases of Si induced by indentation, Phys. Rev. B **83**, 235205 (2011).

[49] T. P. Mernagh and L.-G. Liu, Pressure dependence of Raman phonons of some group IVA (C, Si, and Ge) elements, J. Phys. Chem. Solids **52**, 507 (1991).

[50] V. Paillard, P. Puech, M. A. Laguna, P. Temple-Boyer, B. Caussat, J. P. Couderc, and B. de Mauduit, Resonant Raman scattering in polycrystalline silicon thin films, Appl. Phys. Lett. **73**, 1718 (1998).

[51] V. Paillard, P. Puech, M. A. Laguna, R. Carles, B. Kohn, and F. Huisken, Improved one-phonon confinement model for an accurate size determination of silicon nanocrystals, J. Appl. Phys. **86**, 1921 (1999).

[52] R. W. G. Wyckoff, *Crystal Structures* (Interscience Publishers, New York, 1963), Vol. 1, p. 7.

[53] S. J. Clark, M. D. Segall, C. J. Pickard, P. J. Hasnip, M. I. J. Probert, K. Refson, and M. C. Payne, First principles methods using CASTEP, Z. Kristallogr. **220**, 567 (2005).

[54] A. J. D'Alfonso, B. Freitag, D. Klenov, and L. J. Allen, Atomic-resolution chemical mapping using energy-dispersive x-ray spectroscopy, Phys. Rev. B **81**, 100101(R) (2010).

[55] L. D. Landau and E. M. Lifshitz, *The Classic Theory of Fields* (Pergamon Press, Oxford, 1980).

[56] Y. I. Salamin, S. X. Hu, K. Z. Hatsagortsyan, and C. H. Keitel, Relativistic high-power laser-matter interactions, Phys. Rep. **427**, 41 (2006).

[57] G. A. Mourou, T. S. Tajima, and S. V. Bulanov, Optics at relativistic regime, Rev. Modern Phys. **78**, 309 (2006).

[58] G. Malka and J. L. Miquel, Experimental confirmation of ponderomotive-force electrons produced by an ultrarelativistic laser pulse on a solid target, Phys. Rev. Lett. **77**, 75 (1996).

[59] Y. Kishimoto and T. Tajima, Strong coupling between clusters and radiation, in *High Field Science*, edited by T. Tajima, K. Mima, and H. Baldis (Plenum Press, New York, 1999), p. 83.

[60] W. L. Kruer and K. Estabrook, $J \times B$ heating by very intense laser light, Phys. Fluids **28**, 430 (1985).

[61] P. Gibbon, *Short Pulse Laser Interaction with Matter. An Introduction* (Imperial College Press, London, 2005).

[62] K. B. Wharton, S. P. Hatchett, S. C. Wilks, M. H. Key, J. D. Moody, V. Yanovsky, A. A. Offenberger, B. A. Hammel, M. D. Perry, and C. Joshi, Experimental measurements of hot electrons generated by ultraintense ($> 10^{19}$ W/cm^2) laser-plasma interactions on solid-density targets, Phys. Rev. Lett. **81**, 822 (1998).

[63] M. I. K. Santala, M. Zepf, I. Watts, F. N. Beg, E. Clark, M. Tatarakis, K. Krushelnick, A. E. Dangor, T. McCanny, I. Spencer *et al.*, Effect of the plasma density scale length on the direction of fast electrons in relativistic laser-solid interactions, Phys. Rev. Lett. **84**, 1459 (2000).

[64] A. G. Mordovanakis, P.-E. Masson-Laborde, J. Easter, K. Popov, B. Hou, G. Mourou, W. Rozmus, M. G. Haines, J. Nees, and K. Krushelnick, Temperature scaling of hot electrons produced by a tightly focused relativistic-intensity laser at 0.5 kHz repetition rate, Appl. Phys. Lett. **96**, 071109 (2010).

[65] J. J. Santos, B. Vauzour, M. Touati, L. Gremillet, J.-L. Feugeas, T. Ceccotti, R. Bouillaud, F. Deneuville, V. Floquet, C. Fourment *et al.*, Isochoric heating and strong blast wave formation driven by fast electrons in solid-density targets, New J. Phys. **19**, 103005 (2017).

[66] L. D. Landau, E. M. Lifshitz, and L. P. Pitaevskii, *Electrodynamics of Continuous Media*, 2nd Revised Ed. (Pergamon Press, Oxford, 1984), Chap. 8.

[67] V. T. Tikhonchuk, Inertial confinement fusion—Key elements of plasma physics, in *Encyclopedia of Nuclear Physics*, edited by E. Greenspan (Elsevier, Amsterdam, Netherlands, 2021), Chap. 12, p. 686.

[68] A. R. Bell, J. R. Davies, S. Guerin, and H. Ruhl, Fast-electron transport in high-intensity short-pulse laser-solid experiments, Plasma Phys. Control. Fusion **39**, 653 (1997).

[69] E. J. Boyd and D. Uttamchandani, Measurement of the anisotropy of Young's modulus in single-crystal silicon, J. Micromechanical Systems **21**, 243 (2012).

[70] L. Q. Huston, B. C. Johnston, B. Haberl, S. Wong, J. S. Williams, and J. E. Bradby, Thermal stability of simple tetragonal and hexagonal diamond germanium, J. Appl. Phys. **122**, 175108 (2017).

[71] V. Anand, J. Maksimovic, T. Katkus, S. H. Ng, O. Ulčinas, M. Mikutis, J. Baltrukonis, A. Urbas, G. Šlekys, H. Ogura *et al.*, All femtosecond optical pump and x-ray probe: Holey-axicon for free-electron laser, J. Phys. Photonics **3**, 024002 (2021).

[72] N. Khodakovskiy, M. P. Kalashnikov, E. Gontier, F. Falcoz, and P.-M. Paul, Degradation of picosecond temporal contrast of Ti : sapphire lasers with coherent pedestals, Opt. Lett. **41**, 4441 (2016).

[73] Pulsar TW ultra-intense ultrafast lasers specifications, https://amplitude-laser.com/wp-content/uploads/2020/08/Pulsar-TW-rev-b.pdf.

[74] Y. Azamoum, V. Tcheremiskine, R. Clady, A. Ferré, L. Charmasson, O. Utéza, and M. Sentis, Impact of the pulse contrast ratio on molybdenum Kα generation by ultrahigh intensity femtosecond laser solid interaction, Sci. Rep. **8**, 4119 (2018).

[75] P. K. Singh, Y. Q. Cui, A. Adak, A. D. Lad, G. Chatterjee, P. M. Brijesh, Z. Sheng, and G. R. Kumar, Contrasting levels of absorption of intense femtosecond laser pulses by solids, Sci. Rep. **5**, 17870 (2015).

[76] http://energy.gov/downloads/doe-public-access-plan.

[77] D. N. Nikogosyan, *Properties of Optical and laser-Related Materials: A Handbook* (John Willey and Sons, Chichester, 1997), pp. 318–327.